RESEARCH ARTICLE

The daytime trapped lee wave pattern and evolution induced by two small-scale mountains of different heights

Haile Xue[1,2,3] | Marco A. Giorgetta[2] | Jianping Guo[1]

[1]State Key Laboratory of Severe Weather, Chinese Academy of Meteorological Sciences, Beijing, China

[2]Max Planck Institute for Meteorology, Hamburg, Germany

[3]CMA Earth System Modeling and Prediction Centre (CEMC), Beijing, China

Correspondence
H. Xue, State Key Laboratory of Severe Weather, Chinese Academy of Meteorological Sciences, Beijing, China.
Email: xuehl@cma.gov.cn

Abstract

Two large-eddy simulations are carried out to investigate the vertical structure and daytime evolution of trapped lee waves (TLWs) triggered by mountains of two heights (500 and 1500 m, denoted as HM500 and HM1500, respectively) based on a typical subtropical winter troposphere, in which a steady upper-level jet and a clear diurnal evolution of the atmospheric boundary layer (ABL) are present. Multimode TLWs co-exist at three altitudes with dominant wavelengths increasing with altitude in HM500, while a single-mode TLW dominates throughout most of the troposphere in HM1500. The wave amplitudes for both experiments increase from midday, reaching peaks in the afternoon, likely related to the reduction of the wave absorption by the ABL. Whereas the growth of the dominant wavelength of TLWs with time is mainly limited to layers near the ABL top for HM500; the dominant wavelength in HM1500 stays steady with time. The TLW pattern and evolution can be largely explained by linear theory. In HM500, the multimode pattern is due to the perturbation source at a low altitude where high wavenumbers are supported, and the wavelength length-ening near the ABL top can be explained by the decreasing Scorer parameter in the afternoon. In HM1500, the large-amplitude single-mode TLW is due to the enhanced and elevated perturbation source of the higher mountain where the Scorer parameter is smaller and affected less by the ABL. The continual amplification of the dominant TLW in HM1500 may be caused by the instability from the wave-induced momentum deficit at the upper ABL, which further facilitates the wave propagation. Our findings are beneficial for improving our process-scale understanding of the vertical structure and diurnal evolution of TLWs constrained by the upper-level jet and ABL evolution, and have implications for improving orographic gravity-wave parameterization especially when the model resolution approaches around 10 km.

KEYWORDS
atmospheric boundary layer, diurnal evolution, trapped lee wave, upper-level jet

1 | INTRODUCTION

Trapped lee waves (TLWs) tend to form in stable air flows on the lee side of mountains, notably as the Scorer parameter reduces with altitude (e.g., Scorer, 1949; Durran, 1990). In the lower troposphere, TLWs often induce multiple rows of clouds, such as rotor clouds and lenticular clouds (Li and Chen, 2017; Udina *et al.*, 2017).

Also, some severe downslope windstorms have been recognized to be closely associated with the occurrence of TLWs (Scinocca and Peltier, 1989; Xue *et al.*, 2020). Such storms pose a significant risk for aviation safety (e.g., Darby and Poulos, 2006). The TLWs could result in downward transport of momentum flux from the troposphere to the atmospheric boundary layer (ABL), resulting in the occurrence of rotors when the amplitude is large (Hentenstein and Kuettner, 2005; Doyle and Durran, 2007). However, the large-amplitude TLWs and associated rotors are underrepresented or unresolved in numerical weather prediction (NWP) and climate models (Teixeira *et al.*, 2013a; Xu *et al.*, 2021), which may induce a spurious positive wind bias in the lower troposphere and unrealistic near-surface wind due to the missed momentum transport between upper and lower layers and between upstream and downstream regions (Jiang *et al.*, 2006; Vosper, 2015; Xue and Giorgetta, 2021).

TLW investigation has a long history based on observations (e.g., Gerbier and Berenger, 1961; Lester, 1978; Ralph *et al.*, 1997), theories (Queney *et al.*, 1960; Pearce and White, 1967) and simulations (Jiang and Doyle, 2008; Xue *et al.*, 2020). Long-term subjective cloud observations indicated that TLW-induced clouds occurred more frequently in the afternoon in the cold season in the Jämtland mountains of Sweden (Larsson, 1954) and at Pincher Creek, Canada (Lester, 1978). Among others, the vertical structure of TLW was only observed in a few cases by radar (e.g., Viezee, 1970; Starr and Browning, 1972). Alternatively, TLWs were also observed by means of gliders and radar-tracked balloons (Holmboe and Klieforth, 1957; Gerbier and Berenger, 1961). Aircraft is another major way to observe the vertical structure of TLWs for specific cases (Smith *et al.*, 2002; Chouza *et al.*, 2016; Wagner *et al.*, 2017; Witschas *et al.*, 2017). Satellite images (e.g., Ralph *et al.*, 1997; Li and Chen, 2017) of TLW-induced clouds may also provide useful information but hardly display the vertical structure of the TLW. In recent years, the research focus of TLWs has been shifted toward the wave drag (Bougeault *et al.*, 2001; Smith, 2004; Teixeira *et al.*, 2013a, 2013b) and wave-induced rotors (Grubišić *et al.*, 2008; Strauss *et al.*, 2015). The aforementioned pioneering field campaign studies shed light on the following aspects of TLWs: (a) the wavelength becomes longer during the daytime; (b) the wave amplitude is very small in the presence of a sufficiently stable and stagnant layer and reaches its peak about 1 h before sunset in the presence of a sufficiently unstable and faster-moving ABL; and (c) the wavelength is longer at higher atmospheric levels. However, a continual three-dimensional (3D) direct measurement of TLWs, which would allow a closer study of these three characteristics, remains a daunting challenge, mainly because of the relatively short wavelength of the waves (less than 20 km; Ralph *et al.*, 1997; Grubišić and Billings, 2008; Chouza *et al.*, 2016). As a consequence, the altitude-resolved diurnal evolution of TLWs, to date, is still poorly observed.

Substantial progress has been made in theories and simulations on the diurnal evolution of the TLW amplitude (Smith *et al.*, 2002, 2006; Jiang *et al.*, 2006; Lott, 2007, 2016; Xue and Giorgetta, 2021) with the advent of wave-absorption theory (Smith *et al.*, 2002; Lott, 2007, 2016). The wave-absorption theory manifests an apparent advantage to explain the wave amplification and extension for the existing cases (e.g., Smith *et al.*, 2002; Li and Chen, 2017; Xue *et al.*, 2020) compared to the classical linear theory (e.g., Scorer, 1949; Pearce and White, 1967). Particularly, the wave-absorption theory could adequately consider the absorption and reflection of diurnally evolving TLWs, which is subject to the changes of ABL stability (Jiang *et al.*, 2006; Xue and Giorgetta, 2021). Although the leaky-TLW mechanism related to the stratosphere may also account for the wave amplitude variation (Durran *et al.*, 2015), it cannot explain the diurnal evolution of the TLW. However, these theories cannot well explain the wavelength evolution of TLWs occurring in more realistic conditions. In reality, the upper-level jet (ULJ) is essential for the generation of TLW because it can produce a gradually reducing Scorer parameter (Durran, 1990). Therefore, TLWs and upward propagating waves may co-exist in some layers and those short-wavelength TLWs may only be present in the lower layer because of the high Scorer parameter. However, the classical linear theory (e.g., Pearce and White, 1967) generally treats the atmosphere as a two- or three-layer structure so that the waves are only trapped in lower layers where the Scorer parameter is uniform in the vertical. Moreover, high mountains (i.e., comparable to or higher than the typical ABL depth) tend to induce large-amplitude TLWs where non-linear effects should not be neglected. Such large-amplitude TLWs are generally trapped by a ULJ that reduces the Scorer parameter at the top of the troposphere (Collis *et al.*, 1968; Viezee, 1970; Li and Chen, 2017; Udina *et al.*, 2017; Xue *et al.*, 2020). Our recent simulations show that the variation of the TLW wavelength is found to be closely related to the ULJ that is perpendicular to the ridge of high mountains (Xue and Giorgetta, 2021). Therefore, to investigate the vertical structure and evolution of TLWs under more realistic conditions (e.g., with a gradually reducing Scorer parameter and over mountains of different heights), high-resolution simulations with realistic profiles are necessary.

To this end, in the present study we aim to analyze TLWs associated with an ULJ over mountains of different heights. The purpose is twofold: (a) to elucidate the vertical structures and the variability of TLWs

(e.g., amplitude and wavelength) during daytime; and (b) to investigate the mechanism for how different TLWs evolve over time and space. The remaining parts of this article are organized as follows. The background atmosphere and application of the linear theory are introduced in Section 2. The results of the non-linear simulations are presented in Section 3. The amplification mechanism and influence of TLWs due to a high mountain are discussed in Section 4. Conclusions and summary are given in Section 5.

2 | BACKGROUND ATMOSPHERE AND APPLICATION OF THE LINEAR THEORY

2.1 | Background atmosphere

Since the ULJ is essential for TLWs, it is natural to adopt the subtropical boreal-winter atmosphere over the subtropics as the background because the ULJ is steadily located between 25°N and 35°N (Figure 1a). Numerous
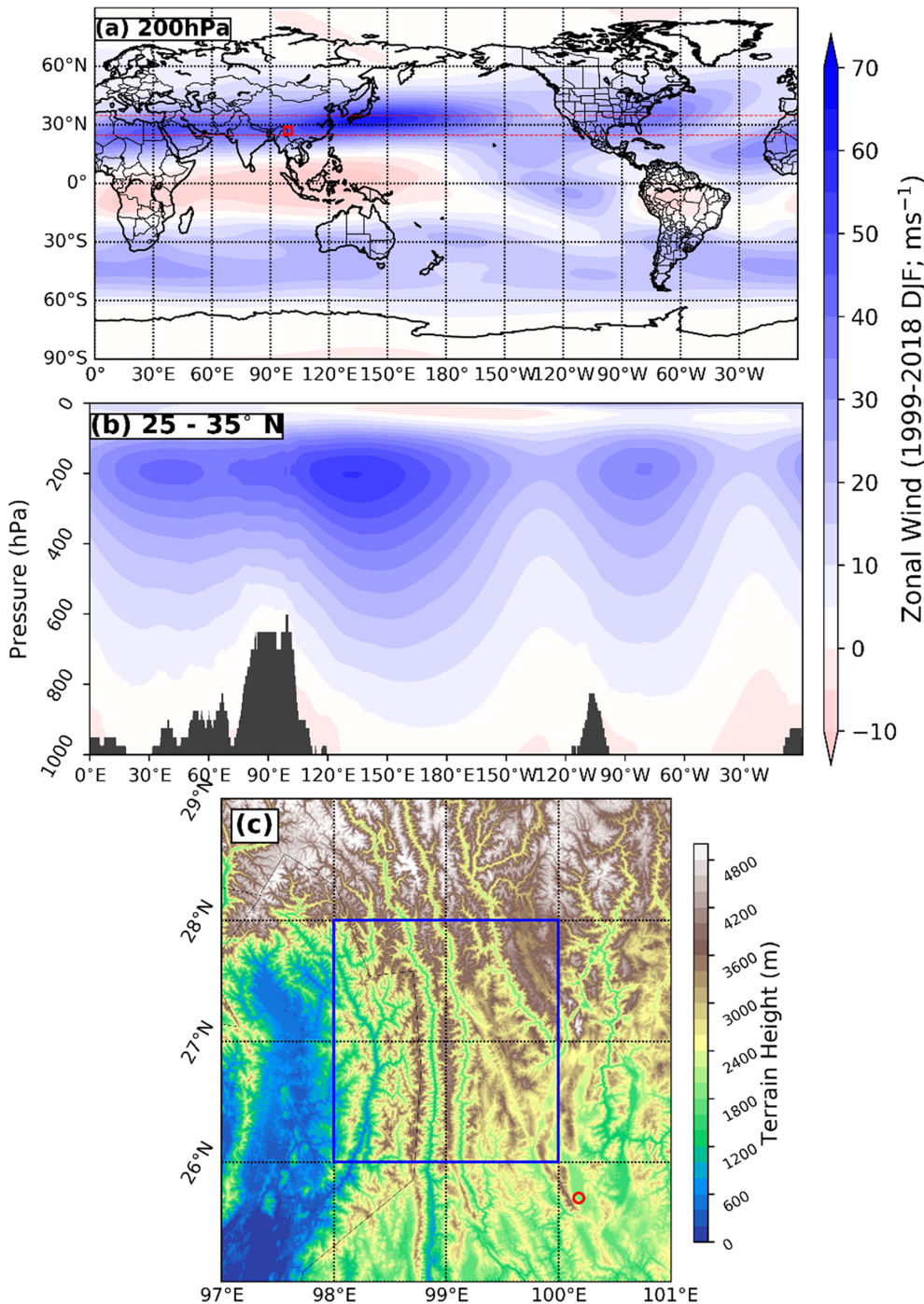

FIGURE 1 Twenty-year mean zonal wind (m·s⁻¹) at (a) 200 hPa and (b) its vertical section averaged between 25°N and 35°N in boreal winter (December–February) from ERA5 reanalysis, and (c) the terrain height (m) of the Hengduan Mountains. The horizontal thin dashed lines (in red) and thick square (in red) in panel (a) indicate the band to be averaged in (b) and the domain for (c), respectively. The topography in (b) is shown in black. The square (in blue) in (c) shows the region to be averaged for profiles in Figure 2, and the circle (in red) in (c) indicates the location of Dali meteorological station, where gales are observed frequently in cold-season afternoons [Colour figure can be viewed at wileyonlinelibrary.com]
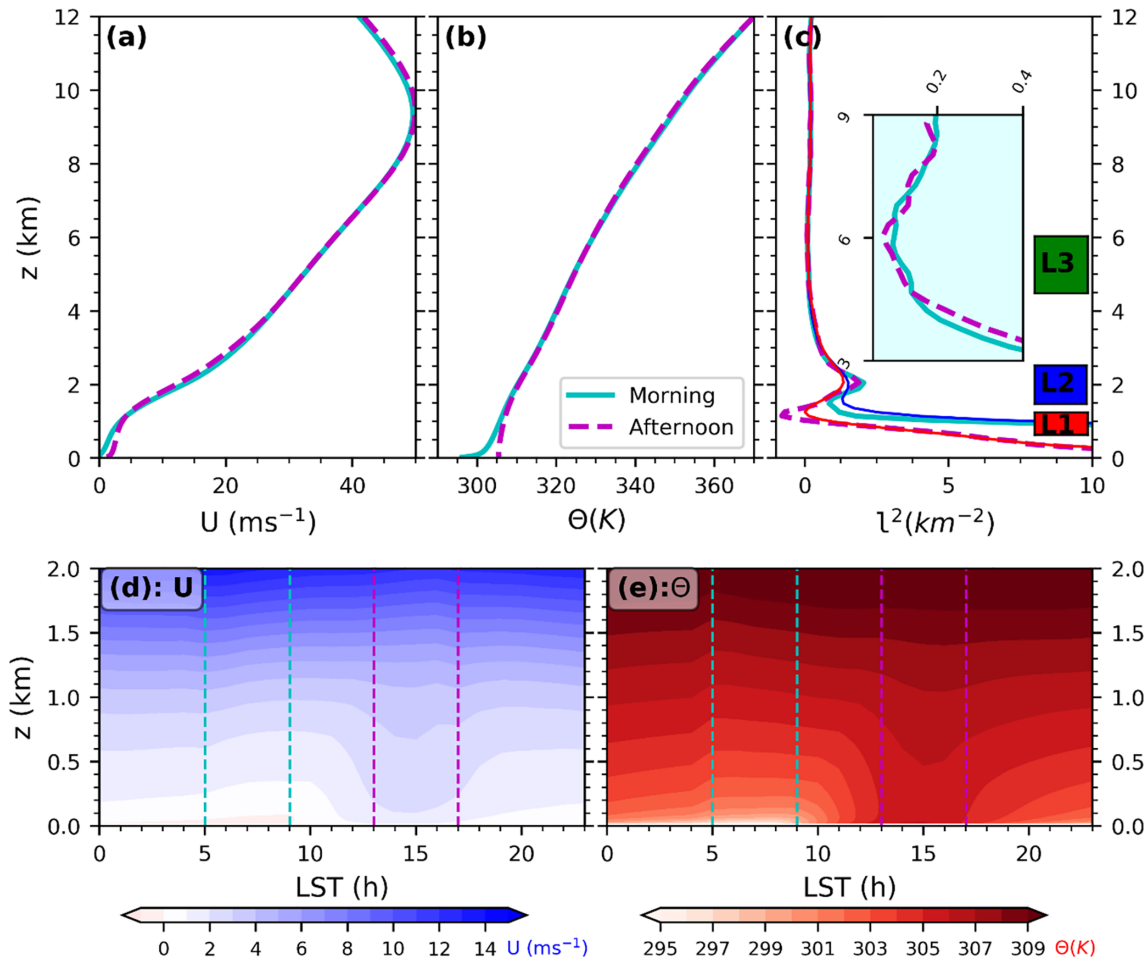
FIGURE 2 Mean profiles of (a) zonal wind (U in m·s^{-1}), (b) potential temperature (Θ in K) and (c) Scorer parameter (l^2 in km^{-2}) from surface to 12 km above ground level, and the diurnal evolution of (d) U and (e) Θ in the lowest 2 km over the Hengduan Mountain region of the southeastern Tibetan plateau. Note that the quantities are extracted from the hourly products of ERA5 reanalysis and averaged over a $2° \times 2°$ domain centered at (27°N, 99°E) for the period from December 2018 to February 2019. The morning hours (05:00 to 09:00 LST [local sidereal time]) and afternoon hours (13:00 to 17:00 LST) in (a–c) are marked in cyan and magenta, respectively in (d) and (e). The blocks on the right side of (c) indicate the vertical extent of the upper atmospheric boundary layer (ABL) (L1; in red), low troposphere layer with a l^2 crest (L2; in blue) and middle troposphere (L3, in green), respectively. The thin red and blue lines in (c) show the smoothed l^2 profile for numerically solving Equations (1)–(3) [Colour figure can be viewed at wileyonlinelibrary.com]

high mountains, such as the Sierra Madre, Himalayas, Hengduan mountains, and Zagros lie under the subtropical ULJ (Figure 1b). Particularly, the Hengduan Mountains (25–28°N, 98–101°E) in the southeastern corner of the Tibetan Plateau, China, are featured by a group of north–south-oriented ridges and valleys with a typical wavelength of 10–30 km (Figure 1c). Gales are frequently observed (one every 3–5 days) on the east of one of the mountains (Dali meteorological station, shown as the red circle in Figure 1c) especially in the afternoon in the cold season based on a 60-year observational statistic (Yang *et al.*, 2013). A case study based on a combination of a realistic large-eddy simulation (LES) and multiple surface observations and wind profiles every 6 min from a radar at Dali meteorological station showed the gale in the afternoon was induced by the amplified TLW (Xue

et al., 2020). Therefore, the background atmosphere over the Hengduan Mountains will be in the focus of the present study.

The winter mean zonal wind (U) and potential temperature (Θ) profiles versus height above ground level (zonal, meridional and vertical directions are denoted as x, y and z, respectively) based on ERA5 reanalysis over the Hengduan Mountains between December 2018 and February 2019 are shown in Figure 2a,b. Both wind and potential temperature are found to vary apparently between morning (05:00–09:00 LST [local sidereal time]) and afternoon (13:00–17:00 LST) hours in the ABL, while the profile hardly varies above the ABL (above about 1.5 km). Therefore, the Scorer parameter, $l^2 = \frac{N^2}{U^2} - \frac{1}{U}\frac{d^2U}{dz^2}$, where N is the buoyancy frequency calculated from Θ, displays a typical three-layer structure above z = 1.5 km in

both morning and afternoon (Figure 2c). This three-layer structure is quite similar to the extensively studied vertical structure (e.g., Vosper, 2004; Teixeira *et al.*, 2013b), in which a temperature inversion is capped on a less stable or neutral ABL and the horizontal wind is assumed to be constant. However, the inversion is absent in our case, but the increasing curvature of the zonal wind with height produces a peak of l^2 at about 2 km that plays a similar role as the inversion in Vosper (2004). The diurnal evolution of the mean zonal wind and mean potential temperature in the ABL shows two clearly different stages (Figure 2d,e). A stable and stagnant layer near the surface is apparent in the morning and a nearly neutral ABL with increased zonal wind is shown in the afternoon. Overall, l^2 decreases with altitude above the ABL in both morning and afternoon, forming a favorable condition for formation of the TLW. Although TLWs are thought to occur occasionally, the above-mentioned observations of gales at Dali and our previous simulations (Xue *et al.*, 2020; Xue and Giorgetta, 2021) indicate that TLWs may occur much more frequently if the ULJ is steadily present over small-scale north–south ridges. Therefore, the winter mean profiles shown in Figure 2 serve as background atmosphere to investigate the diurnal variation of TLWs. To facilitate the analysis, three layers are defined to represent: (a) very high l^2 in the upper ABL between 0.8 and 1.2 km, denoted as L1; and (b) a lower troposphere layer characterized by a l^2 peak playing a similar role as the inversion between 1.5 and 2.5 km, denoted as L2; and (c) a middle troposphere layer where l^2 reduces to its minimum at the top of this layer between 4.5 and 6.0 km, denoted as L3 respectively (Figure 2c).

2.2 | Application of the linear theory

Following Shutts (1992), the vertical amplitude structure of a single-plane harmonic wave is governed by the well-known equation

$$\frac{d^2\widehat{w}}{dz^2} + \left(l^2 - k^2\right)\widehat{w} = 0 \tag{1}$$

where $\widehat{w}$ is the complex vertical structure function in the following expression for the vertical velocity $w(x, z)$:

$$w(x, z) = \text{real}\{\widehat{w}(z)\exp(ikx)\}$$

with k defined as the horizontal wavenumber. The radiation boundary condition is applied at the top as

$$\frac{d\widehat{w}}{dz}\left(z = z_{\text{top}}\right) = im\widehat{w}\left(z = z_{\text{top}}\right) \tag{2}$$

where $m = \left(l^2 - k^2\right)^{1/2}$ is the vertical wavenumber. The lower boundary condition is

$$\widehat{w}_{\text{low}} = ikU_0\widehat{h} \tag{3}$$

where U_0 is the surface wind speed and $\widehat{h}$ is the Fourier transform of the topography. For a 2-D bell-shaped mountain

$$h(x) = \frac{h_{\text{m}}}{1 + (x/a)^2} \tag{4}$$

$$\widehat{h} = \frac{h_{\text{m}}a}{2}e^{-a|k|} \tag{5}$$

where h_{m} is the maximum mountain height and a represents the half-width of the mountain. For a realistic atmosphere, the viscosity cannot be neglected, thus $U_0 = 0$ on the ground surface. Teixeira *et al.* (2004) suggested that the "surface wind" to use in the inviscid model should perhaps be that in the middle or upper part of the ABL based on a boundary layer scaling analysis by Belcher and Wood (1996). The maximum level that is affected by the ABL in the present study is at about 1.2 km as illustrated by the zonal wind and potential temperature profiles in Figure 2, so U_0 at 0.8 km is used as the "surface wind." Alternatively, Shutts (1997) adopted a "wave-launching height" at 1 km in his study which is close to the 0.8 km in our study. h_{m} and a are set as 20 m and 3000 m (slightly wider than a cosine mountain profile of 12-km wavelength) respectively, to ensure the linear perturbation ($H_N = h_{\text{m}}U_0/N \ll 1$) and gentle slope ($h_{\text{m}}/a \ll 1$). Equations (1)–(3) can be solved as a boundary-value problem given various k (or wavelength $\lambda = 2\pi/k$) and l^2. To solve the problem numerically, a second-order Gaussian smoother is applied on the l^2 profiles for the morning and afternoon (thin blue and red line, respectively, Figure 2c).

Figure 3 shows the vertical profiles of normalized wave amplitude ($|\widehat{w}|/|\widehat{w}_{\text{low}}|$) solved from Equations (2) and (3) with a "wave-launching height" at 0.8 km. Generally, the propagating waves with longer wavelength (18 km $\leq \lambda$) are identified with peaks at the altitude of about 10 km, and the shorter gravity waves (6 km $\leq \lambda \leq 16$ km) are trapped below about 6 km. The very short ($\lambda \leq 4$ km) gravity waves are evanescent as $|\widehat{w}|/|\widehat{w}_{\text{low}}|$ rapidly decreases to zero from the bottom to about 3 km. These results are as expected by the linear theory and consistent with existing studies (e.g., Shutts, 1992; Teixeira *et al.*, 2013a). However, many details are displayed with these solutions. First, when the waves are trapped, the maximum $|\widehat{w}|/|\widehat{w}_{\text{low}}|$ for different wavelength is at different altitude. For example, the maximum $|\widehat{w}|/|\widehat{w}_{\text{low}}|$ for $\lambda = 6$ km is at about 1 km in our L1, but that for $\lambda = 8$ km is at about
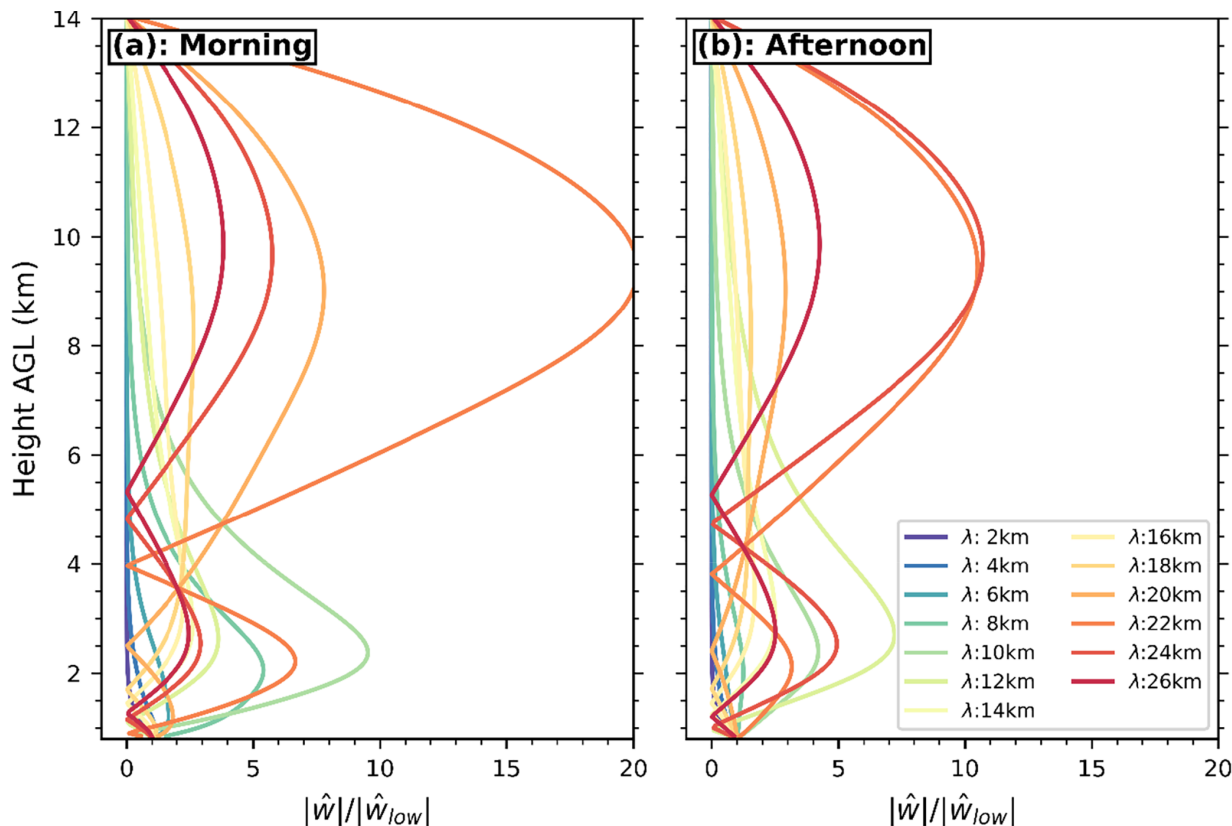
FIGURE 3 Vertical profiles of normalized wave amplitude solved from Equations (1)–(3) given lower boundary condition at 800 m for various wavelengths ($\lambda = 2\pi/k$) and l^2 in the (a) morning and (b) afternoon. AGL, above ground level [Colour figure can be viewed at wileyonlinelibrary.com]

$z = 2$ km in L2 in the morning. Second, the wavelength of the dominant TLW in the morning is about 10 km, but it increases to 12 km in the afternoon. These results indicate that the lower layers (L1 and L2) may be dominated by shorter TLWs but the upper layers (L2 and L3) may be co-dominated by longer TLWs and propagating waves.

As the Scorer parameter varies with height, the wave pattern and evolution may be sensitive to the "wave-launching height" which is further related to the mountain height. First, as the "wave-launching height" becomes higher, the longer waves may be triggered and the shorter waves are no longer supported with a smaller Scorer parameter at that level. Second, the atmosphere at higher altitude is less affected by the ABL, so the dominant wave mode varies less diurnally. Third, as the background wind increases with height in the lower troposphere, $\hat{w}_{low}$ will largely increase with mountain height and thus $\hat{h}$. Therefore, large-amplitude TLWs may be generated and be dominant throughout the lower troposphere. To support this interpretation, Figures 4 and 5 show the vertical profiles of $|\hat{w}|/|\hat{w}_{low}|$ but with a "wave-launching height" at 600 m and 1000 m respectively. To focus on TLWs, the propagating waves of λ longer than 16 km are

excluded. When the "wave-launching height" is 600 m, the dominant TLW mode has a wavelength of 6 km and its morning peak is in L1 (Figure 4a). In the afternoon, the dominant TLW mode has a wavelength of 12 km and its peak is in L2 (Figure 4b). When the "wave-launching height" increases to 1 km, the dominant TLW mode has a wavelength of 12 km and its peak is in L2 in the morning and afternoon (Figure 5). Furthermore, the amplitude of the dominant mode is increased when the "wave-launching height" is increased from 600 m to 1 km (Figures 4 and 5), especially in the afternoon. These results show that the pattern and evolution of TLWs are sensitive to the mountain height in a realistic atmosphere, in which the wind speed usually increases with height in the troposphere.

3 | NON-LINEAR SIMULATION

3.1 | Experiment design

The fully compressible ICOsahedral Non-hydrostatic (ICON) model is adopted to run the non-linear simulations, which uses an unstructured triangular grid with
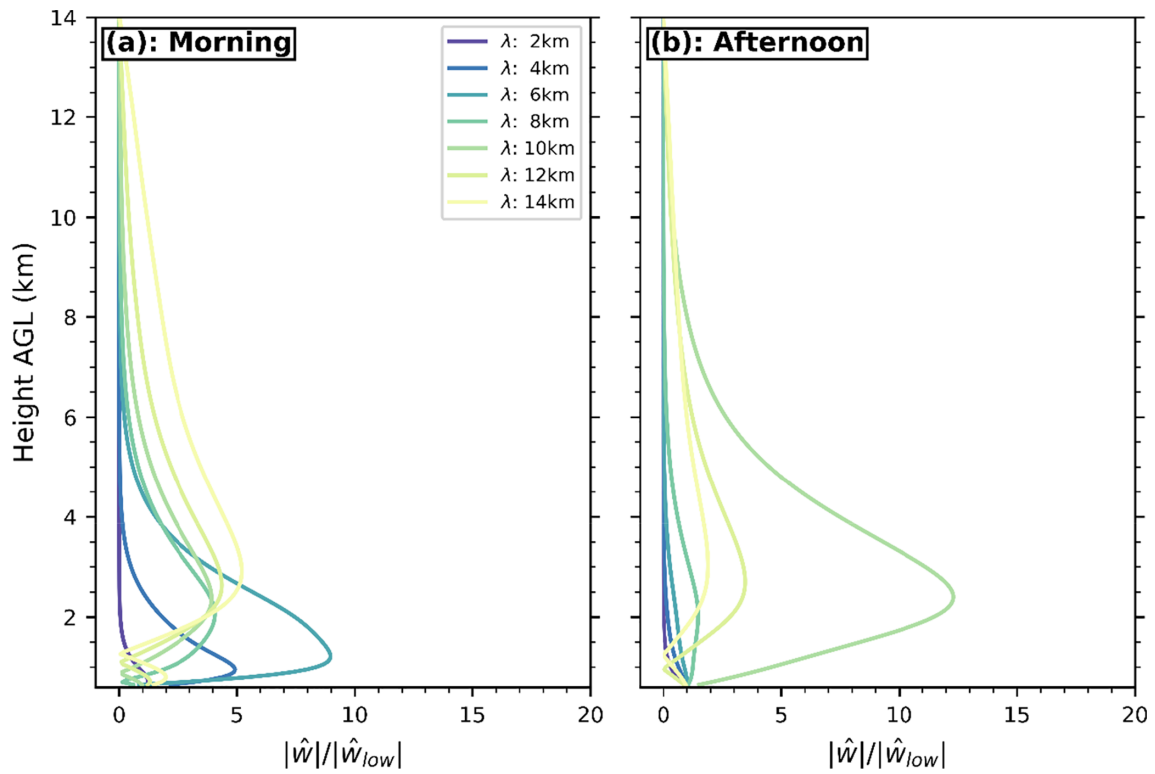
FIGURE 4   Same as Figure 3, but with the lower boundary condition at 600 m [Colour figure can be viewed at wileyonlinelibrary.com]
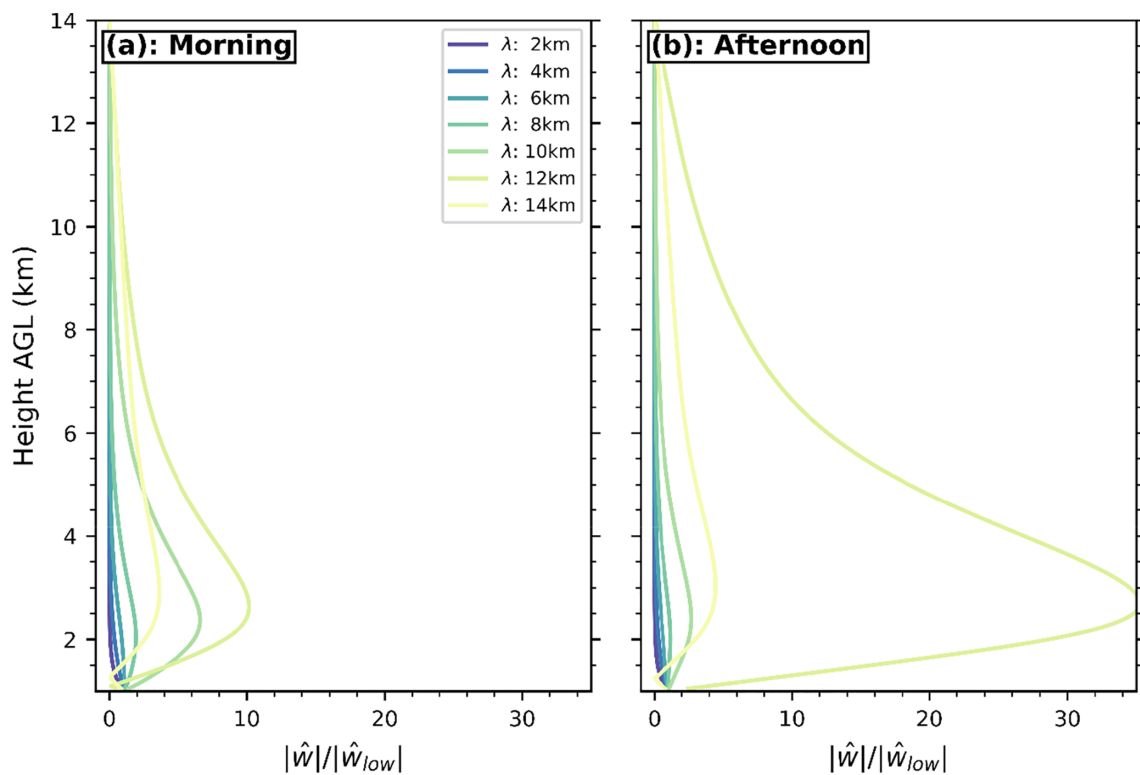

FIGURE 5   Same as Figure 3, but with the lower boundary condition at 1 km [Colour figure can be viewed at wileyonlinelibrary.com]

C-type staggering and a height-based terrain-following coordinate system (Zängl *et al.*, 2015; Giorgetta *et al.*, 2018). For our study the ICON model is configured for large-eddy simulations (ICON-LES), as it has been demonstrated before that such simulations can serve as a high-fidelity tool for studying the influence of the ABL on development of the mountain wave (Smith and Skyllingstad, 2009; 2011; Sauer *et al.*, 2016). Further, such a model allows to simulate the diurnal evolution of the ABL that is essential for the issue under investigation in the present study. The ICON-LES model uses a modified Smagorinsky scheme to parameterize the unresolved turbulence and thermal stratification (Lilly, 1962; Dipankar *et al.*, 2015; Baldauf and Brdar, 2016; Heinze *et al.*, 2017). The performance of the ICON-LES configuration has been validated for cases with idealized flat surface (Dipankar *et al.*, 2015), idealized steep topography (Xue and Giorgetta, 2021) and realistic atmosphere and topography (Heinze *et al.*, 2017). For our investigation, a rectangular domain with a length (x axis) and width (y axis) of 204.8 and 2.6 km, respectively, is used with a grid of triangular cells of 50-m edge length. An infinitely-long mountain in the y direction is set in the domain with its peak at the center of the x direction. The terrain height is formulated as Equation (4) but with $h_\text{m} = 500$ m and $h_\text{m} = 1500$ m to represent low and high mountains, respectively. For the sake of simplification, the simulations corresponding to these two mountain settings are denoted as HM500 and HM1500. Following Vosper (2004), periodic lateral boundary conditions are used in both x and y directions, but damping columns is applied at the beginning and end of the x axis, at the inflow and outflow boundaries, respectively. The damping columns efficiently maintain the specified inflow and damp gravity waves that flow from the outflow boundary to the inflow boundary due to the periodic boundary condition (Xue and Giorgetta, 2021). Therefore, the time-varying profiles shown in Figure 2a,b can be set as inflow conditions to account for the time evolution of the background atmosphere. In the vertical direction, Rayleigh damping on vertical wind following Klemp *et al.* (2008) is applied in the top 19-km layer to prevent reflection of gravity waves at the model top. The vertical grid uses stretched vertical layers with depth ranging from $\Delta z = 7$ m at the surface to $\Delta z = 533$ m at the model top at 30 km height. The roughness length is set as 0.1 m. More details of the model configuration can be found in Xue and Giorgetta (2021).

Since night-time observations of TLWs are rare, we only focus on waves at daytime. The two simulations ran from 05:00 LST to 21:00 LST. Simulation of the first 4 h of this period covers the spin-up phase, and is therefore not evaluated. It has been shown that the turbulence can be well developed in both upstream and downstream regions (Xue and Giorgetta, 2021). Figure 6a,b shows the x–z cross-section of snapshots of w for both HM500 and HM1500 at 14:00 LST when the turbulence is important. Turbulence is shown in both upstream and downstream regions for the two mountain settings. As expected, the turbulent kinetic energy (TKE) spectra follow an approximate $k^{-5/3}$ power law (Figure 6c), and most of the TKE is confined in the lowest layer below $z = 0.5$ km except for a peak at about $z = 1$ km for the HM1500 (Figure 6d) that is likely induced by the shear between the blocked layer and the air skimming over and above it. Note that the blocking effect may reduce the effective mountain height as the background near-surface wind speed is very low. In the following, all results will be averaged in the y direction as the periodic boundary condition is applied and the mountain is homogeneous in the y direction.

3.2 | Results

3.2.1 | Vertical structure of the TLW

Figure 7a shows the x–z cross-section of the vertical velocity normalized with a reference vertical velocity, $W_\text{N} = \max\{U[h(x)]\partial h(x)/\partial x\}$, and potential temperature over the period from 09:00 to 21:00 LST, to represent the mean state in the whole daytime, here for the HM500 experiment. It can be seen that very small perturbations are present below $z = 1$ km on the lee side. Overall, different wave modes are present at different layers (Figure 7b). In particular, L1 is characterized by the shortest wavelength, as compared to the longest observed in L3. The mean power spectra show dominant TLW modes of shortest wavelength in L1 and of longest wavelength in L3 (Figure 7c). These results from the non-linear LES of HM500 are quite similar to the linear solutions especially when the "wave-launching height" is low, i.e., the higher wavenumber waves are trapped in the lower layer and the lower wavenumber TLWs and propagating waves are present in the upper layer. Similar wave patterns have also been previously observed in the Black Mountains in Wales (Starr and Browning, 1972) and in the Alps (Gerbier and Berenger, 1961).

A similar analysis is done for HM1500 (Figure 7d–f). A striking feature is that the dominant TLW wavelength (approximately 12 km) does not change with altitude (Figure 7e–f). This is noticeably contrary to the multimode TLW structure from HM500 but consistent with the linear solution when the "wave-launching height" is high. Similar vertical structures of TLWs have also been frequently observed and simulated over high mountains (Li and Chen, 2017; Udina *et al.*, 2017; Xue *et al.*, 2020). As for the amplitude, although it is much larger in HM1500
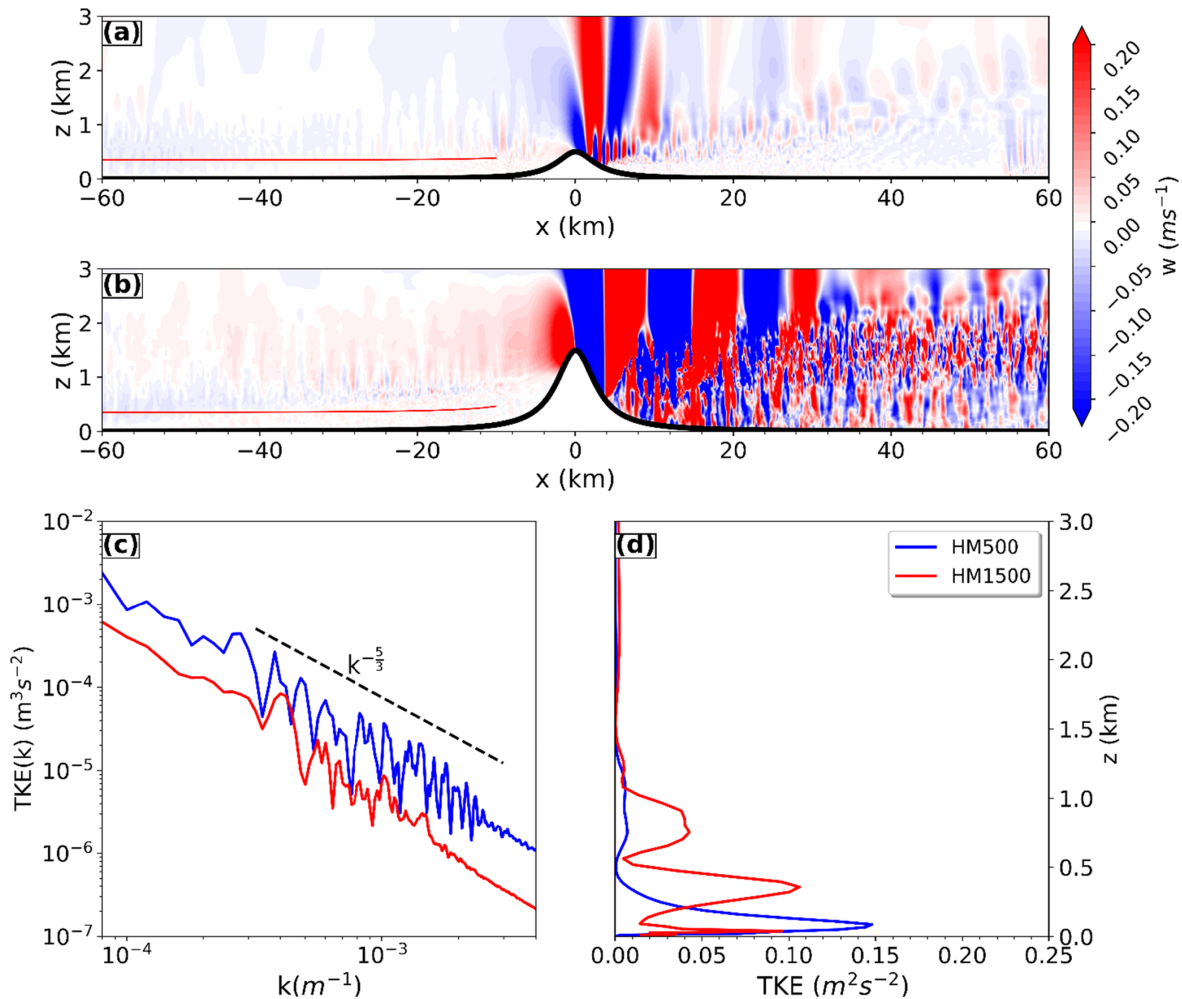
FIGURE 6 Distance (x)–altitude (z) cross-section of instantaneous vertical velocity (w; in m·s^{-1}) at (a) mountain height in meters b(HM)-500 and (b) HM1500 at 14:00 LST (local sidereal time), and the upstream (c) turbulent kinetic energy (TKE) spectra at a height of about 360 m (indicated by the thin red lines) and (d) TKE profiles averaged between −60 and −30 km [Colour figure can be viewed at wileyonlinelibrary.com]

than in HM500 (i.e., W_N is 0.13 and 1.6 m·s^{-1} in HM500 and HM1500, respectively), its normalized magnitude is similar in both experiments (Figure 7a,d). This indicates that the wave amplitude may be linearly dependent on the source perturbation from the mountain, that is, the product of the background wind speed and mountain slope. It is surprising that the non-linear effect may play a less important role even in the HM1500 experiment with a mean slope of $\frac{h_m}{a} = 0.5$ compared to that in hydraulic-jump lee waves (e.g., Smith, 1985; Durran, 1986). Our off-line diagnosis shows that the magnitude of non-linear terms is one order magnitude smaller than the linear terms in the vertical momentum equation (not shown). Therefore, for a high mountain (e.g., $h_m = 1500$ m), the large-amplitude TLW may be initiated by the strong upslope force and propagates horizontally to the downstream with a dominant wavelength governed by the Scorer parameter near the mountain top and above.

3.2.2 | Diurnal variability of the TLW

Figure 8 illustrates the diurnal variation of power spectra of normalized vertical velocity in the daytime in the three layers for both experiments. The magnitude of the power spectra (color shadings in Figure 8) represents the mean amplitude of gravity waves between $x = -10$ km and $x = 40$ km, and the ordinate in Figure 8 denotes the wavelength. The mean amplitude tends to increase in the afternoon (from around 13:00 LST) for all wave modes in all three layers. This result is partly consistent with linear solutions, in which only the dominant wave mode is amplified in the afternoon (Figures 4 and 5). The ABL wave absorption/reflection mechanism may be taken into account for this discrepancy. Under the influence of solar radiation, the ABL starts to grow unstable after sunrise and reaches its peak in the afternoon, which is generally thought of as convective ABL (e.g., Guo *et al.*, 2016;
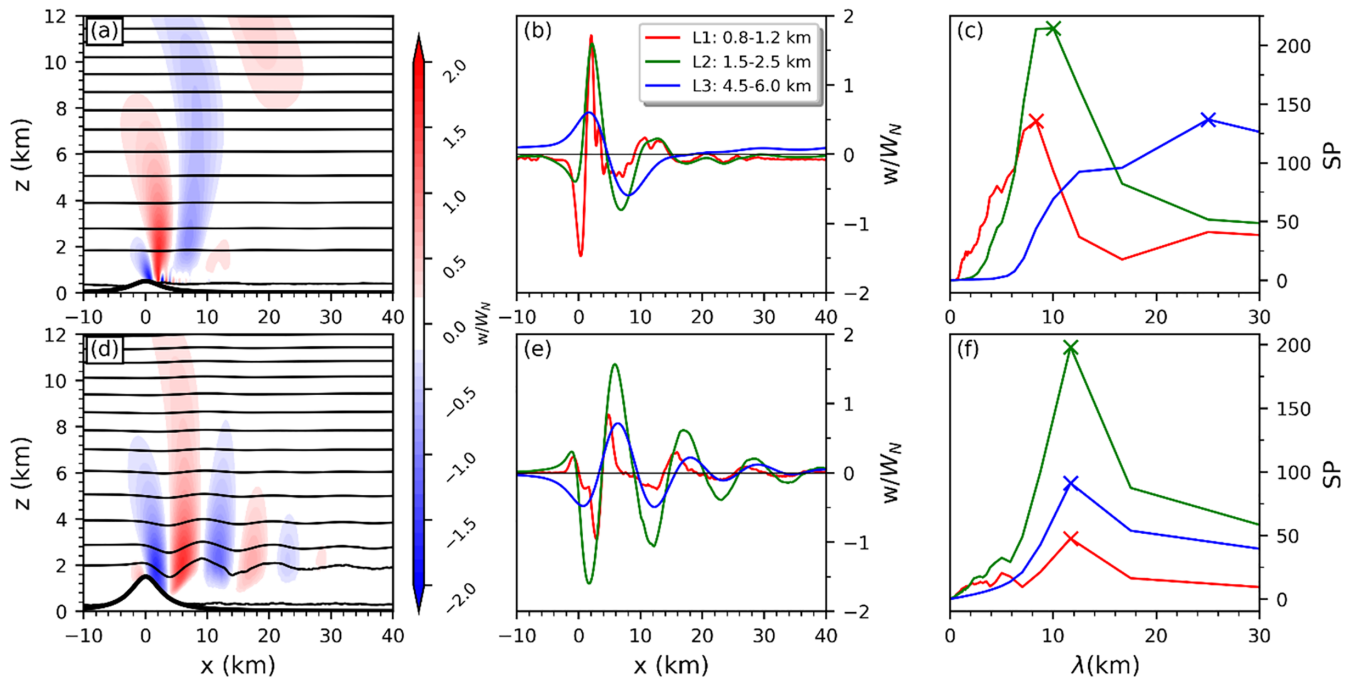
FIGURE 7 Distance (x)–altitude (z) cross-section of normalized vertical velocity (w/W_N; color shaded; unitless), and potential temperature (θ; contour lines at 5 K intervals) for the experiment (a) mountain height in meters (HM)-500 and (d) HM1500. Panels (b) and (c) show the averaged w/W_N and its power spectra (SP), respectively, for three layers (L1, L2, L3) of the HM500 experiment. Panels (e, f) are the same as (b, c), but for the HM1500 experiment. The reference vertical wind is defined as the maximum perturbation of vertical velocity at the surface as $W_N = \max\{U[h(x)]\partial h(x)/\partial x\}$, which is 0.13 and 1.6 m·s^{-1} for HM500 and HM1500, respectively. All the quantities are calculated separately at 10-min intervals and then averaged over the period 09:00–21:00 LST (local sidereal time) [Colour figure can be viewed at wileyonlinelibrary.com]

Zhang *et al.*, 2018). The convective ABL has been shown to reflect TLWs with a low decaying ratio that leads to a wave amplification (Smith *et al.*, 2002; Jiang *et al.*, 2006; Lott, 2007; Xue and Giorgetta, 2021). However, the wave amplification in HM1500 (Figure 8b,d,f) is sustained for more time than that in HM500 (Figure 8a,c,e). The amplification sometimes can continue in the night (Li and Chen, 2017; Xue *et al.*, 2020) for which we have no simulations available. However, the evolution of the wavelength is dependent on the layers and mountain heights. For the low-mountain case HM500, the dominant wavelength is shifted apparently from shorter wavelengths in the morning to longer wavelengths in the afternoon in L1 (Figure 8e) and L2 (Figure 8c). The increase of the dominant wavelength in lower layers in HM500 in the afternoon can be well explained by the decrease of the Scorer parameter (l^2) in the lower layers (Figure 2c). Although the dominant wavelength in L3 almost stays steady with $\lambda = 25$ km indicating a vertically propagating wave (Figure 8a), TLWs seem to be co-existing in the layer as the power spectra of shorter wavelengths increase in the afternoon, which is qualitatively consistent with the linear solution shown in Figure 3. By contrast, the dominant wavelength in HM1500 stays steady for all three

layers throughout the simulation period (Figure 8b,d,f), which is more similar to the linear solution for a higher "wave-launching height" (Figure 5).

4 | DISCUSSION

4.1 | Implication of TLW for local circulation and model parameterizations

One of the most important impacts of gravity waves on the mean circulation is to vertically transport horizontal momentum between the free atmosphere and the ABL (Eliassen and Palm, 1960), while the turbulence mixing may become important in the ABL if rotors are induced (Turnipseed *et al.*, 2004; Doyle and Durran, 2007). Figure 9 shows the cross-section of the resolved vertical momentum flux ($\tau w = \overline{\rho} \overline{u'w'}$) scaled by h_m^2 and TKE for the two experiments, where the variables with primes are the perturbation from the horizontal mean with overbars and ρ is the density. Both wave-induced momentum flux and rotor-induced turbulence are much larger and of a larger extension in the downstream region of the high mountain (Figure 9b,d). It is also noticed that the scaled τ_w is even
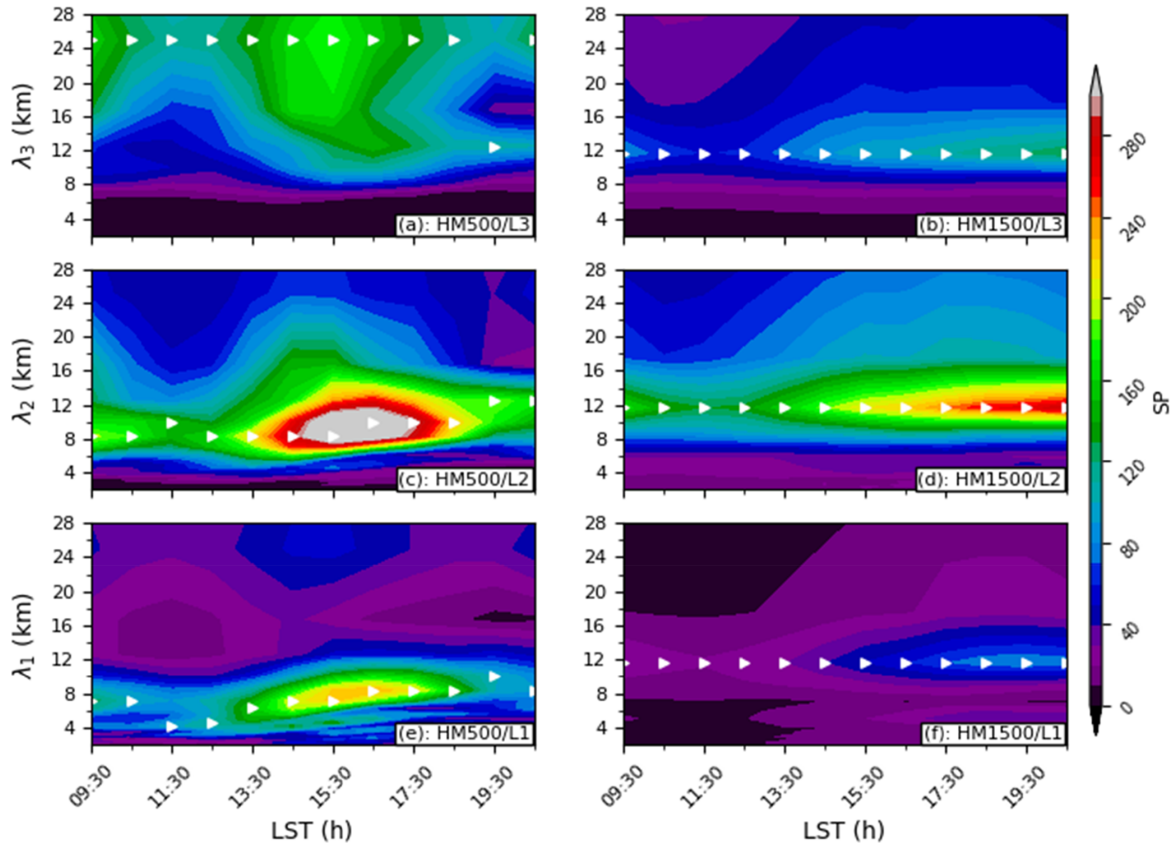
FIGURE 8 Temporal evolution of power spectra (SP) of w/W_N (unitless) during daytime in the three layers of L1, L2 and L3 for both experiments, mountain height in meters (HM)-500 (a,c,e) and HM1500 (b,d,f). The spectral analyses are conducted at 1-h intervals which are based on 10-min simulation results between $x = -10$ km and $x = +40$ km. The white triangle markers indicate the dominant wavelength corresponding to the maximum amplitude of the power spectrum for each hour, LST, local sidereal time [Colour figure can be viewed at wileyonlinelibrary.com]

larger in the afternoon than in the morning for the two experiments (Figure 9c,d).

To better interpret the wave's influence on the mean flow, a well-established method for the horizontal mean τ_w of the TLW is adopted (Broad, 2002; Jiang *et al.*, 2006; Xue and Giorgetta, 2021). Defining a horizontal averaging operator as $\langle M_{m,n} \rangle = \int_{x_m}^{x_n} M dx$ from x_m to x_n ($x_m < x_n$), the horizontal mean momentum flux for the steady, inviscid, and irrotational flow can be written as

$$\frac{\partial \langle \tau_{wm,n} \rangle}{\partial z} = \frac{\overline{\rho}}{2} w'^2 (x_n, z) - \frac{\overline{\rho}}{2} w'^2 (x_m, z) \qquad (6)$$

where x_m (x_n) is a position sufficiently far on the upstream side of the mountain, or a downstream position where w' is maximum (one of the wave crests for w'; $x_m < x_n$), and x_n is a position sufficiently far on the downstream side. Letting $x_m = x_0 \rightarrow -\infty$ where $w' = 0$, and $x_n = x_1$ for the first crest of w', Equation (6) is rewritten as

$$\frac{\partial \langle \tau_{w0,1} \rangle}{\partial z} = \frac{\overline{\rho}}{2} w'^2 (x_1, z) \qquad (7)$$

Since $\frac{\overline{\rho}}{2} w'^2 (x_1, z) > 0$ and $\frac{\partial \overline{\rho} u'}{\partial t} \propto -\frac{\partial \langle \tau_{w0,1} \rangle}{\partial z}$, the TLW tends to decelerate the flow above the ABL between x_0 and x_1. Moreover, $\langle \tau_{w0,1} \rangle$ tends gradually to zero in the upper troposphere due to the wave reflection thus is negative between the upper troposphere and ABL. Because $\langle \tau_{w0,1} \rangle$ is zero at the surface as the wind speed is null due to the ABL's viscosity and surface friction, $-\frac{\partial \langle \tau_{w0,1} \rangle}{\partial z}$ must be positive in the ABL. Therefore, the TLW tends to accelerate the flow in the ABL between x_0 and x_1. Note that the complexity of the TLW–ABL interaction should be taken into account where viscosity becomes important, so the analysis cannot be used in the ABL directly. However, the viscosity is usually important in the "inner region" near the surface and scaled as $\frac{u_*}{U_0} a$ (Belcher *et al.*, 1993) that is about 150 m and thus much thinner than the typical ABL and troposphere, if the friction velocity $u_* \sim 0.5$ m · s^{-1} and the "surface wind" $U_0 \sim 10$ m · s^{-1}. Therefore, the overall effect of the TLW on the ABL based on the above analysis is valid if the "inner region" is assumed as a thin layer. Similarly, let $x_m = x_1$ for the first crest of w', and
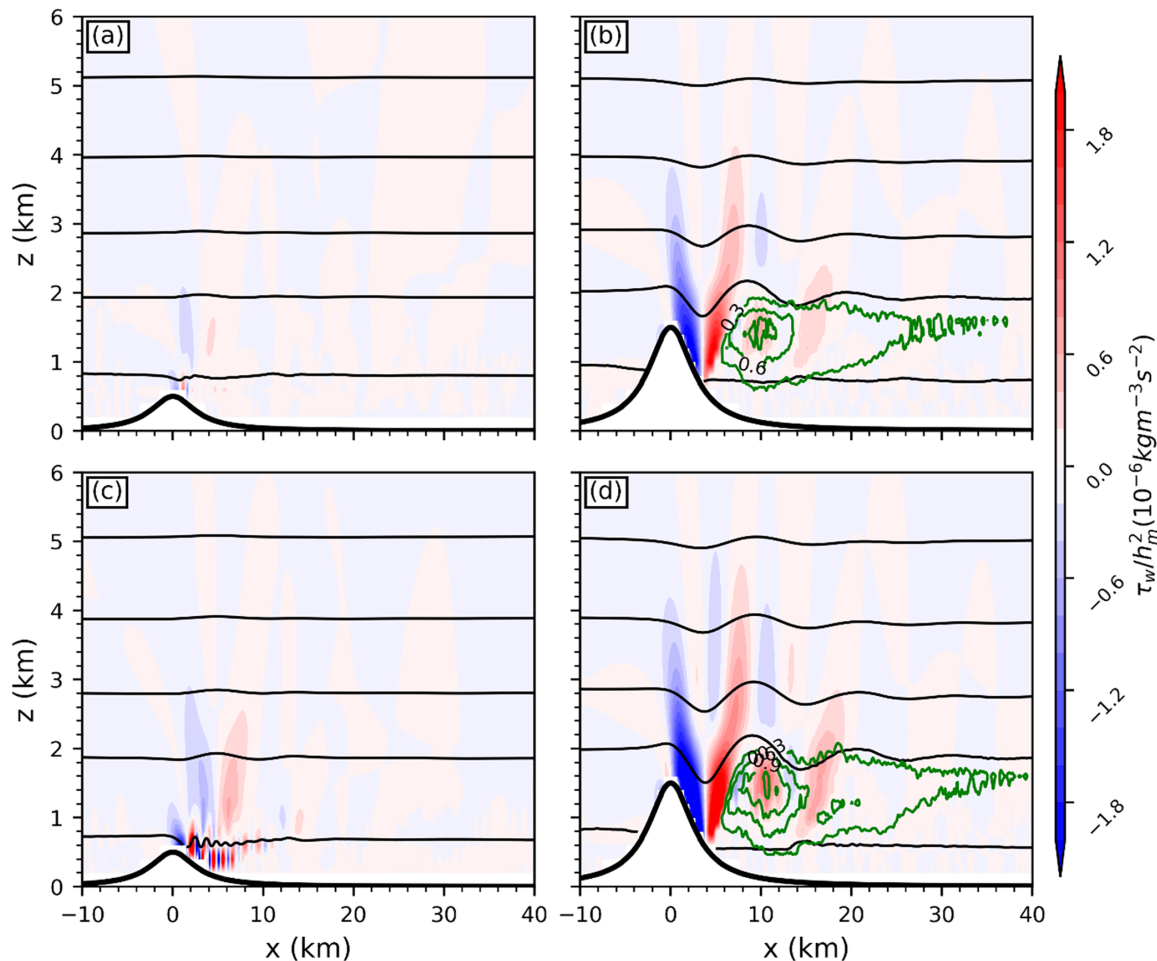
FIGURE 9 Distance (x)–altitude (z) cross-section of the resolved vertically transported horizontal momentum flux (τ_w) scaled by the square of mountain height (h_m^2; in kg·m^{-3}·s^{-2}; color-shaded) and turbulent kinetic energy (TKE; green contours with interval of 0.3 m^2·s^{-2}) for both experiments, (a) mountain height in meters (HM)-500 and (b) HM1500, between 10:00 and 11:00 LST (local sidereal time). Panels (c) and (d) are the same as (a) and (b), respectively, but between 15:00 and 16:00 LST. θ is displayed for reference as contour lines at 5 K intervals [Colour figure can be viewed at wileyonlinelibrary.com]

$x_n = x_2 \rightarrow \infty$. Then, Equation (6) can be rewritten as

$$\frac{\partial \langle \tau_{w1,2} \rangle}{\partial z} = -\frac{\overline{\rho}}{2} \overline{w'^2}(x_1, z) \qquad (8)$$

Therefore, the TLW tends to accelerate the flow above the ABL between x_1 and x_2 as $-\frac{\overline{\rho}}{2}\overline{w'^2}(x_1, z) < 0$. Again, $\langle \tau_{w1,2} \rangle$ tends gradually to zero in the upper troposphere thus it is positive between the upper troposphere and the ABL. Therefore, the TLW tends to decelerate the flow in the ABL between x_1 and x_2 because $\langle \tau_{w1,2} \rangle$ is zero at the surface. Finally, let $x_m = x_0 \rightarrow -\infty$, and $x_n = x_2 \rightarrow \infty$, which yields

$$\frac{\partial \langle \tau_{w0,2} \rangle}{\partial z} = 0 \qquad (9)$$

Equation (9) indicates that the average influence of the TLW on the mean circulation in a large domain is zero.

This means that the pressure drag exerted by the mountain acts on the downstream ABL through the TLWs which are reflected by the upper layer (say the ULJ) and gradually absorbed by the downstream ABL. Therefore, the integration is zero if its extension between the integration boundaries includes the momentum sink and source together. Note that the conclusion does not contradict with existing studies, for example Teixeira *et al.* (2013a, 2013b), in which the surface pressure drag is non-zero. The surface pressure drag is deduced from TLWs without ABL absorption, which may be balanced by the momentum term on the left side of Equation (7). However, when the absorption of the ABL is taken into account, a counterpart pressure force with opposite direction is generated due to the reduction of the amplitude from the ABL absorption as shown in Equation (8). Therefore, the surface pressure drag of TLWs is offset by an opposite pressure force in the
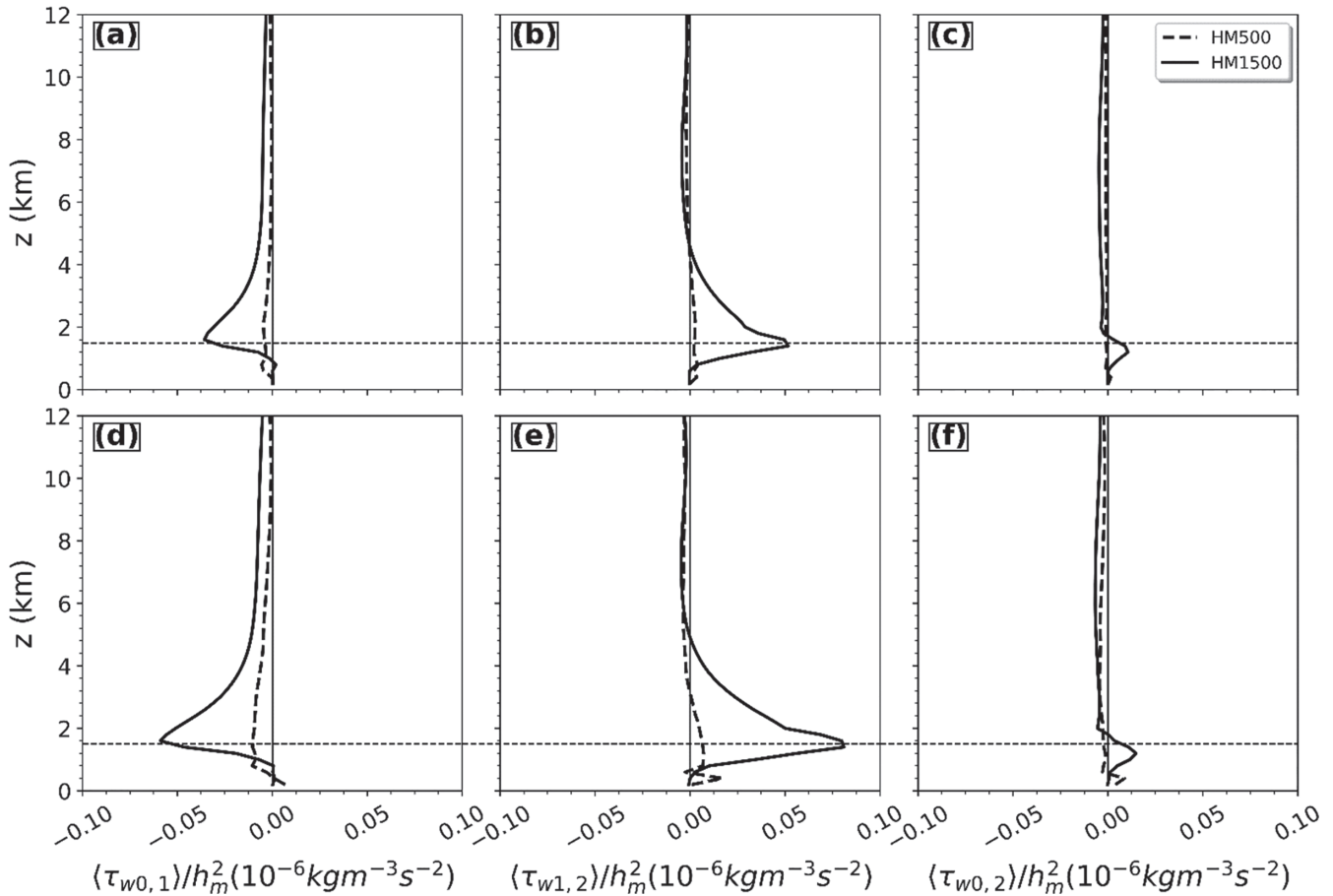
FIGURE 10 The mean τ_w scaled by $h_m{}^2$ (in kg·m^{-3}·s^{-2}) between 10:00 and 11:00 LST (local sidereal time) (a–c) and between 15:00 and 16:00 LST (d–f). Here, $<\tau_{wm,n}>$ refers to the momentum flux integrated from x_m to x_n. The integration boundaries are $x_0 = -60$ km, x_1 is the position of the first crest of w' for L2, and $x_2 = +60$ km. The horizontal dashed line shows the bottom height of L2 for reference

downstream region. This should be considered with care if the conclusion applies in the near-surface flow, where the viscosity becomes important (Teixeira, 2017).

In our simulation, x_0 and x_2 are set as -60 km and $+60$ km, respectively, where w' is much smaller compared to the first crest of w'. Figure 10 shows the mean $\langle\tau_{w0,1}\rangle$, $\langle\tau_{w1,2}\rangle$, and $\langle\tau_{w0,2}\rangle$ profiles averaged between x_0 and x_1 (the position of the first wave crest of w'), between x_1 and x_2, and between x_0 and x_2. Here, $\langle\tau_{w0,1}\rangle$ and $\langle\tau_{w1,2}\rangle$ are negative and positive, respectively, with the peaks just above the ABL as predicted by Equations (7) and (8). However, $\langle\tau_{w0,2}\rangle$ is much smaller than $\langle\tau_{w0,1}\rangle$ and $\langle\tau_{w1,2}\rangle$ but not zero. The non-zero $\langle\tau_{w0,2}\rangle$ is likely caused by the upward-propagating waves, which are nearly constant in height between the ABL top and 10 km. The propagating waves, with wavelengths larger than 16 km, are supported based on the linear solutions in Section 2.2. Moreover, based on the observations during the Deep Propagating Gravity Wave Experiment (DEEPWAVE) campaign, it was found that the non-hydrostatic waves of shorter wavelength ($\lambda = 8$–15 km) carried little horizontal momentum

flux (Smith *et al.*, 2016; Smith and Kruse, 2017). This is consistent with the results from the linear model and non-linear simulations in our case. The TLW leakage mechanism (Durran *et al.*, 2015) may also contribute, but the leakage wave pattern (e.g., Figure 6 in Durran *et al.*, 2015) is not shown in our study (Figure 7a,d). Note that a momentum flux peak is shown in the upper ABL (Figure 10c,f). This may be caused by the asymmetric forces between $-\frac{\partial\langle\tau_{w0,1}\rangle}{\partial z}$ and $-\frac{\partial\langle\tau_{w1,2}\rangle}{\partial z}$. In the lee, TLWs can extend to the surface so that the force could act on the lower ABL; in the downstream region, the TLWs are ducted between the ABL and the ULJ, so that the wave absorption may occur mainly in the upper ABL. This can be shown by the perturbation zonal wind in Figure 11, in which positive (negative) perturbation zonal wind is shown in the lee surface (upper ABL in the downstream). It can be summarized as follows: the horizontal momentum is transported from the middle troposphere to the ABL over the mountain region, but it is transported back from the ABL to the layer above over the downstream region. Thus, wind in the layer above the ABL tends to
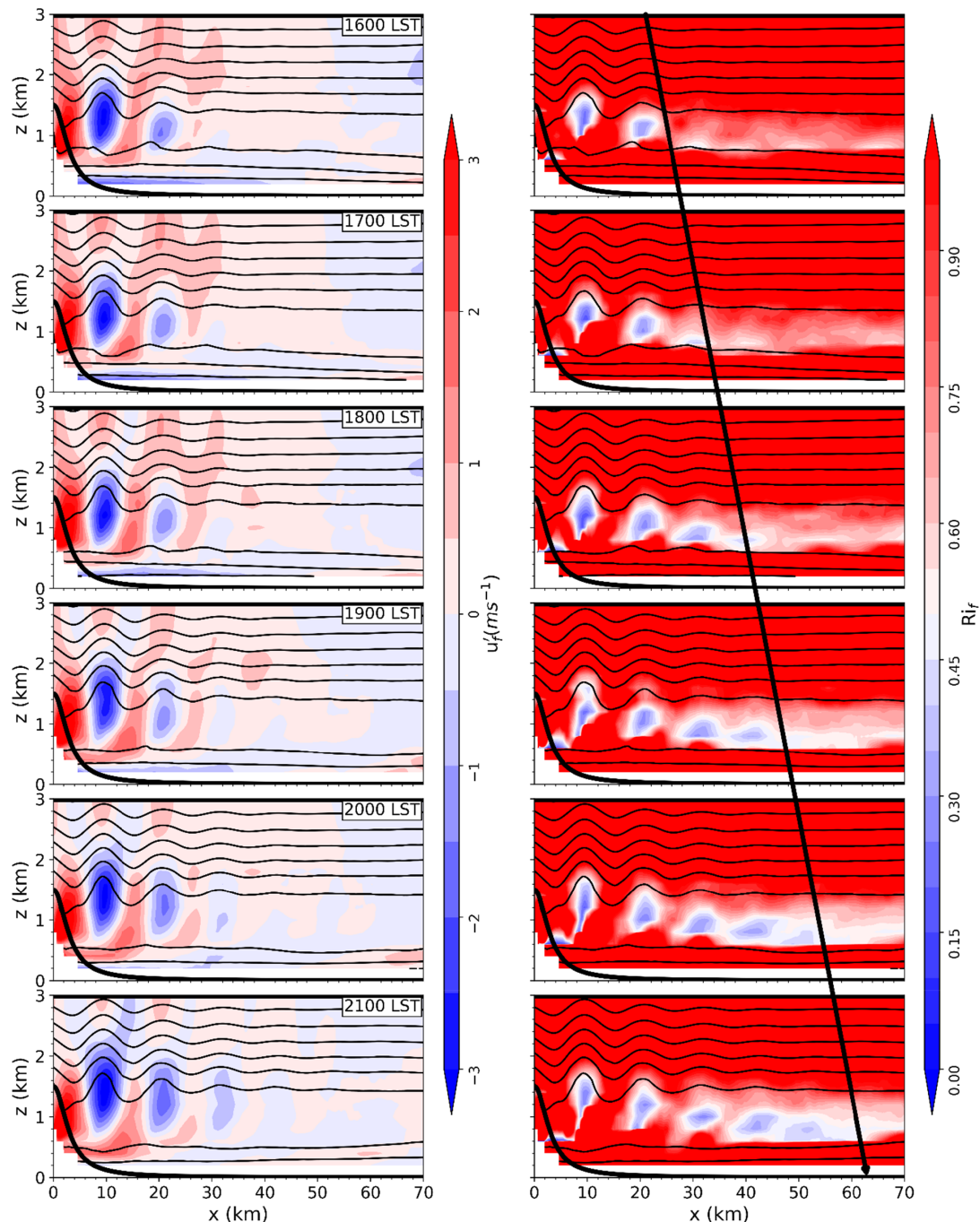
FIGURE 11   Distance (x)–altitude (z) cross-sections of hourly u'_f (left column; in m·s^{-1}) and Ri_f (right column; unitless) between 16:00 and 21:00 LST (local sidereal time). θ is displayed for reference as contour lines at 5 K intervals. The thick black line with arrow shows the extension of the trapped lee waves (TLWs) with time [Colour figure can be viewed at wileyonlinelibrary.com]

be decreased over the mountain, accompanied by the generation of downslope wind and rotors in the lee, while the above-mentioned reverse flow may be formed in the ABL in the downstream region.

The distribution of the TLW-induced momentum flux may introduce a large difficulty in the orographic gravity parameterization as the model resolution increases. When the resolution is coarse (of about 100-km grid size),

the average momentum flux above the ABL tends to zero if we assume the TLWs decay dramatically at the edge of the grid box. However, when the grid size is reduced to about 10 km or less, the poorly-resolved momentum will have a larger impact on the resolved flow than at lower resolutions. If a grid box is centered on the mountain, the wind in the ABL and middle troposphere may be underestimated and overestimated, respectively. If a
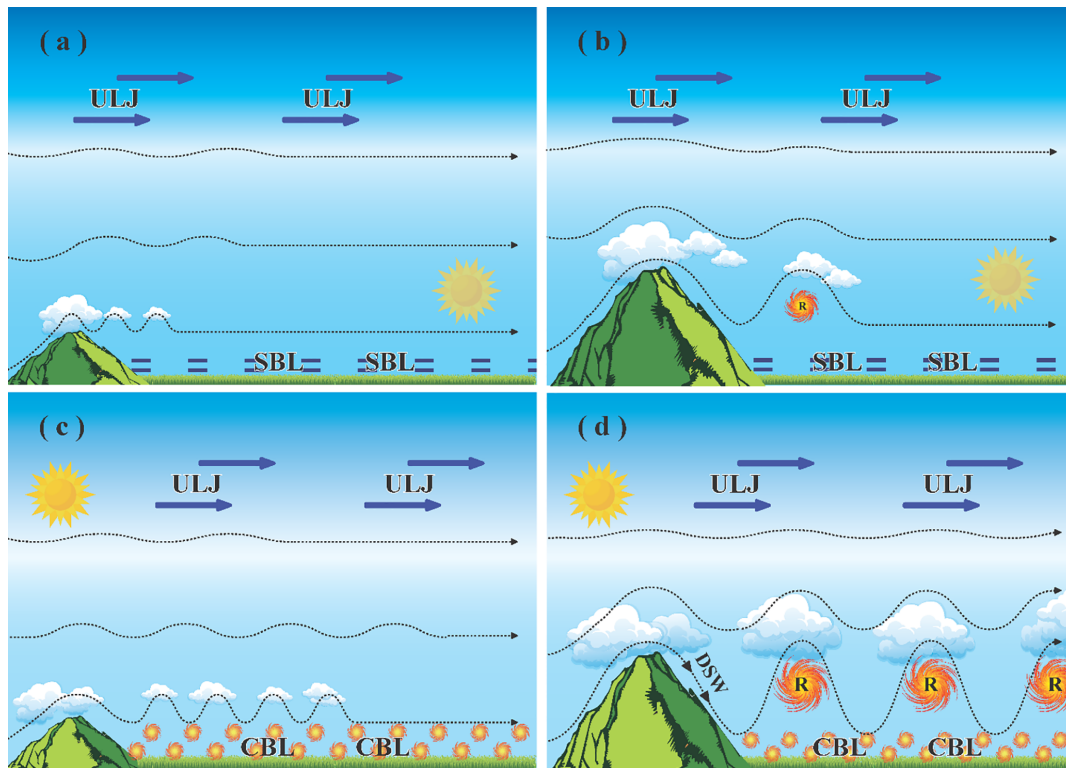
FIGURE 12   Sketch diagram for (a,c) the multimode TLWs in mountain height in meters (HM)-500 and (b, d) single-mode TLWs in HM1500 with the presence of the diurnal ABL evolution and ULJ. (a, b) Smaller amplitude with shorter extension of TLWs due to the wave absorption of the SBL in the morning and (c, d) larger amplitude and longer extension of TLWs due to the wave reflection of the CBL in the afternoon are shown. ABL, atmospheric boundary layer; CBL, convective boundary layer; DSW, downslope wind; R, rotor; SBL, stable boundary layer; TLW, trapped lee wave; ULJ, upper-level jet [Colour figure can be viewed at wileyonlinelibrary.com]

grid box is downstream of the mountain, the wind in the ABL and middle troposphere may be overestimated and underestimated, respectively. Since the TLW propagates horizontally, it creates a difficulty for the parameterization which is usually applied locally in independent columns. However, the local TLW-induced momentum flux is much larger than the propagating-wave momentum flux in our simulations and varies largely with time and mountain height (Figures 9 and 10). The local weather may be largely influenced by high small-scale mountains. Further, as indicated earlier, the atmospheric condition for the TLW may be easily satisfied especially in the cold season over the subtropics in the northern hemisphere, where the ULJ is steadily located. TLWs may occur widely over those mountainous regions. Therefore, how to parameterize TLWs and associated rotors in models of about 10-km resolution or less requires more research.

4.2 | Continual amplification mechanism of the TLW after sunset

The wave pattern and evolution in the HM500 experiment are consistent with the linear solutions presented in Section 2.2, and the wave amplification can also be interpreted with the wave absorption/reflection theory (Smith *et al.*, 2006; Lott, 2007). However, based on the wave absorption theory, the TLW amplitude should be decreasing as the ABL recovers its stability after 17:00 LST (Figure 2d,e) as found in HM500 (Figure 8a,c,e). However, a continual amplification of the TLW is found in HM1500 (Figure 8b,d,f). We suspect that the wind shear and stability in the ABL may be modified by large-amplitude TLWs as presented in Section 4.1, which may facilitate horizontal wave propagation. A parameter related to the leeward wave propagation is the filtered Richardson number, $Ri_f = N_f^2/(\partial u_f/\partial z)^2$, which is calculated locally from the filtered buoyancy frequency N_f and filtered wind u_f shear (here we used a running mean with a window length of 6 km as the filter in the x direction). If the local and large-scale instabilities refer to Richardson numbers calculated from the atmospheric fields in HM1500 and background profiles in Figure 2, respectively, Ri_f represents an instability induced by TLWs of scales between the local and large scales. When the mountain is high, a strong wind shear can be produced between the layer dominated by TLWs and the ABL where the reverse flow may be generated (Soufflet *et al.*, 2019; Xue and

Giorgetta, 2021). This is shown as a negative filtered wind (u'_f) at a height of about 1 km in Figure 11 (left column). The wave-induced shear produces a low-value Ri_f that may reduce the supposed wave absorption due to the stabilized ABL after the sunset. The hourly $x–z$ cross-section of Ri_f between 16:00 and 21:00 LST shows a low value Ri_f (<0.5) at a height of about 1 km and extending downstream with time in Figure 11 (right column). Therefore, TLWs can propagate further downstream, resulting in an increase of the mean amplitude. This can be interpreted as follows: as the large-amplitude TLW forced by the high mountain propagates horizontally downstream, the self-induced low-value Ri_f at the interface between the TLW-dominated layer and the ABL can facilitate the wave propagating further downstream, resulting in a continual increase of the mean amplitude over a considerable downstream distance despite of the stabilization of the ABL after sunset.

5 | CONCLUSIONS AND SUMMARY

A winter mean profile of wind and temperature over the Hengduan Mountains on the southeastern Tibetan Plateau is used to force a channel flow over a small-scale mountain, using two different mountain heights. The background atmosphere is characterized by a diurnal and vertical variation of the ABL Scorer parameter. Three layers, the upper ABL, and the low and the middle troposphere, are defined to analyze the wave structure and evolution in daytime at different altitudes. The simulations allowed the conditions under which the lengthening of the wavelength and amplification of TLWs occur to be constrained. A sketch diagram is shown in Figure 12. In the low-mountain experiment (HM500), multiple-mode TLWs are found with wavelength increasing with height (Figure 12a,c). The dominant wavelength becomes longer in the afternoon in the upper ABL and low troposphere but stays steady in the middle troposphere in HM500 (Figure 12a,c). The multimode TLW structure resulting from the low-mountain experiment is qualitatively consistent with the linear solution of a lower "wave-launching height." The daytime evolution of the wavelength in the lower layers is also supported by the linear theory as the Scorer parameter decreases from the morning to the afternoon due to the increase of the wind speed and decrease of the buoyancy frequency. In the high-mountain experiment (HM1500), a single-mode TLW is dominant through all layers (Figure 12b,d), which is also supported by the linear solution of a higher "wave-launching height." Concerning the amplitude, an increase in the afternoon is found for the two experiments and three layers, which can be partly explained by the diurnal evolution of the ABL,

which is destabilized by solar heating from the morning to the afternoon. Based on the wave absorption/reflection theory (Smith *et al.*, 2006; Lott, 2007), the TLW is absorbed or reflected by the ABL under stable or unstable conditions respectively, so that the mean wave amplitude increases in the afternoon. However, the period of the wave amplification in the HM1500 experiment is much longer even though the ABL's stability increases after 17:00 LST, which is diagnosed as the result of the self-induced low-value Richardson number between the ABL and the layer above that facilitates propagation of the wave. As the TLWs and rotors are strong for high mountains especially in the afternoon (Figure 12b,d), the TLW-induced momentum flux and rotor-induced turbulence may significantly modify the wind field over mountainous region. Based on the findings, the vertical structure and evolution of TLWs over subtropical mountainous regions are displayed and the potential influence of large-amplitude TLWs on the momentum flux and TKE is discussed, which indicates a large part of the momentum flux may be missed if the model resolution is too coarse to resolve the TLW.

AUTHOR CONTRIBUTIONS

Haile Xue: Conceptualization; data curation; formal analysis; investigation; methodology; software; validation; visualization; writing – original draft; writing – review and editing. **Marco Giorgetta:** Funding acquisition; project administration; software; supervision; writing – review and editing. **Jianping Guo:** Writing – review and editing.

ORCID

Haile Xue https://orcid.org/0000-0003-4774-7059
Marco A. Giorgetta https://orcid.org/0000-0002-4278-1963

REFERENCES

Baldauf, M. and Brdar, S. (2016) 3D diffusion in terrain-following coordinates: testing and stability of horizontally explicit, vertically implicit discretizations. *Quarterly Journal of the Royal Meteorological Society*, 142, 2087–2101. https://doi.org/10.1002/qj.2805.

Belcher, S.E. and Hunt, J.C.R. (1993) Turbulent shear flow over slowly moving waves. *Journal of Fluid Mechanics*, 251, 109–148.

Belcher, S.E. and Wood, N. (1996) Form and wave drag due to stably stratified turbulent flow over low ridges. *Quarterly Journal of the Royal Meteorological Society*, 122, 863–902.

Bougeault, P., Binder, P., Buzzi, A., Dirks, R., Houze, R., Kuettner, J., Smith, R.B., Steinacker, R. and VoIkert, H. (2001) The MAP special observing period. *Bulletin of the American Meteorological Society*, 82, 433–462. https://doi.org/10.1175/1520-0477(2001)082<0433:TMSOP>2.3.CO;2.

Broad, A.S. (2002) Momentum flux due to trapped lee waves forced by mountains. *Quarterly Journal of the Royal Meteorological Society*, 128, 2167–2173.

Chouza, F., Reitebuch, O., Jähn, M., Rahm, S. and Weinzierl, B. (2016) Vertical wind retrieved by airborne lidar and analysis of Island induced gravity waves in combination with numerical models and in situ particle measurements. *Atmospheric Chemistry and Physics*, 16, 4675–4692. https://doi.org/10.5194/acp-16-4675-2016.

Collis, R.T.H., Fernald, F.G. and Alder, J.E. (1968) Lidar observations of Sierra-wave conditions. *Journal of Applied Meteorology*, 7, 227–233.

Darby, L.S. and Poulos, G.S. (2006) The evolution of mountain waves and rotors in the lee of Pike's peak under the influence of a cold front: implications for aircraft safety. *Monthly Weather Review*, 134, 2857–2876. https://doi.org/10.1175/MWR3208.1.

Dipankar, A., Stevens, B., Heinze, R., Moseley, C., Zängl, G., Giorgetta, M. and Brdar, S. (2015) Large eddy simulation using the general circulation model ICON. *Journal of Advances in Modeling Earth Systems*, 7, 963–986. https://doi.org/10.1002/2015MS000431.

Doyle, J.D. and Durran, D.R. (2007) Rotor and subrotor dynamics in the lee of three-dimensional terrain. *Journal of the Atmospheric Sciences*, 64, 4202–4221. https://doi.org/10.1175/2007JAS2352.1.

Durran, D.R. (1986) Another look at downslope windstorms. Part I: the development of analogs to supercritical flow in an infinitely deep, continuously stratified fluid. *Journal of the Atmospheric Sciences*, 43(21), 2527–2543.

Durran, D.R. (1990) Mountain waves and downslope winds. In: *Atmospheric Processes over Complex Terrain*. Vol 23. Boston: American Meteorological Society, pp. 59–81.

Durran, D.R., Hills, M.O.G. and Blossey, P.N. (2015) The dissipation of trapped lee waves. Part I: leakage of inviscid waves into the stratosphere. *Journal of the Atmospheric Sciences*, 72(4), 1569–1584. https://doi.org/10.1175/JAS-D-14-0238.1.

Eliassen, A. and Palm, E. (1960) On the transfer of energy in stationary mountain waves. *Geophysical Research Letters*, 22(3), 1–23.

Gerbier, N. and Berenger, M. (1961) Experimental studies of lee waves in the French Alps. *Quarterly Journal of the Royal Meteorological Society*, 87, 13–23. https://doi.org/10.1002/qj.49708737103.

Giorgetta, M., Brokopf, R., Crueger, T., Esch, M., Fiedler, S., Helmert, J., Hohenegger, C., Kornblueh, L., Köhler, M., Manzini, E., Mauritsen, T., Nam, C., Raddatz, T., Rast, S., Reinert, D., Sakradzija, M., Schmidt, H., Schneck, R., Schnur, R., Silvers, L., Wan, H., Zängl, G. and Stevens, B. (2018) ICON-A: the atmospheric component of the ICON earth system model. Part I: model description. *Journal of Advances in Modeling Earth Systems*, 10, 1613–1637. https://doi.org/10.1029/2017MS001242.

Grubišić, V. and Billings, B.J. (2008) Climatology of the Sierra Nevada Mountain-wave events. *Monthly Weather Review*, 136, 757–768. https://doi.org/10.1175/2007MWR1902.1.

Grubišić, V., Doyle, J.D., Kuettner, J., Mobbs, S., Smith, R.B., Whiteman, C.D., Dirks, R., Czyzyk, S., Cohn, S.A., Vosper, S., Weissmann, M., Haimov, S., De Wekker, S.F.J., Pan, L.-L. and Chow, F.K. (2008) The terrain-induced rotor experiment. *Bulletin of the American Meteorological Society*, 89(10), 1513–1534.

Guo, J., Miao, Y., Zhang, Y., Liu, H., Li, Z., Zhang, W., He, J., Lou, M., Yan, Y., Bian, L. and Zhai, P. (2016) The climatology of planetary boundary layer height in China derived from radiosonde and reanalysis data. *Atmospheric Chemistry and Physics*, 16, 13309–13319.

Heinze, R., Dipankar, A., Henken, C.C., Moseley, C., Sourdeval, O., Tromel, S., Xie, X., Adamidis, P., Ament, F., Baars, H., Barthlott, C., Behrendt, A., Blahak, U., Bley, S., Brdar, S., Brueck, M., Crewell, S., Deneke, H., Di Girolamo, P., Evaristo, R., Fischer, J., Frank, C., Friederichs, P., Göcke, T., Gorges, K., Hande, L., Hanke, M., Hansen, A., Hege, H.-C., Hoose, C., Jahns, T., Kalthoff, N., Klocke, D., Kneifel, S., Knippertz, P., et al. (2017) Large-eddy simulations over Germany using ICON: a comprehensive evaluation. *Quarterly Journal of the Royal Meteorological Society*, 143, 69–100. https://doi.org/10.1002/qj.2947.

Hentenstein, R.F. and Kuettner, J.P. (2005) Rotor types associated with steep lee topography: influence of the wind profile. *Tellus A: Dynamic Meteorology and Oceanography.*, 57(2), 117–135. https://doi.org/10.3402/tellusa.v57i2.14625.

Holmboe, J. and Klieforth, H. (1957) *Investigations of Mountain Lee Waves and Airflow over the Sierra Nevada*. Final Report, Contract AF19(604)-728, University of California AD No. 133606. Los Angeles, CA: Department of Meteorology, University of Califonia, p. 290.

Jiang, Q. and Doyle, J.D. (2008) On the diurnal variation of mountain waves. *Journal of the Atmospheric Sciences*, 65(4), 1360–1377. https://doi.org/10.1175/2007JAS2460.1.

Jiang, Q., Doyle, J.D. and Smith, R.B. (2006) Interaction between trapped waves and boundary layers. *Journal of the Atmospheric Sciences*, 63, 617–633. https://doi.org/10.1175/JAS3640.1.

Klemp, J.B., Dudhia, J. and Hassiotis, A.D. (2008) An upper gravity-wave absorbing layer for NWP applications. *Monthly Weather Review*, 136, 3987–4004. https://doi.org/10.1175/2008MWR2596.1.

Larsson, L. (1954) Observations of lee wave clouds in the Jämtland Mountains, Sweden. *Tellus*, 6, 124–138. https://doi.org/10.1111/j.2153-3490.1954.tb01102.x.

Lester, P.F. (1978) A lee wave cloud climatology for pincher creek, Alberta. *Atmosphere-Ocean*, 16, 157–168.

Li, L. and Chen, Y. (2017) Numerical simulations of two trapped mountain lee waves downstream of Oahu. *Journal of Applied Meteorology and Climatology*, 56, 1305–1324. https://doi.org/10.1175/JAMC-D-15-0341.1.

Lilly, D.K. (1962) On the numerical simulation of buoyant convection. *Tellus*, 14(2), 148–172. https://doi.org/10.3402/tellusa.v14i2.9537

Lott, F. (2007) The reflection of a stationary gravity wave by a viscous boundary layer. *Journal of the Atmospheric Sciences*, 64, 3363–3371. https://doi.org/10.1175/JAS4020.1.

Lott, F. (2016) A new theory for downslope windstorms and trapped mountain waves. *Journal of the Atmospheric Sciences*, 73, 3585–3597. https://doi.org/10.1175/JAS-D-15-0342.1.

Pearce, R.P. and White, P.W. (1967) Lee wave characteristics derived from a three-layer model. *Quarterly Journal of the Royal Meteorological Society*, 93, 155–165. https://doi.org/10.1002/qj.49709339602.

Queney, P., Corby, G.A., Gerbier, N., Koschmieder, H. and Zierep, J. (1960) *The Airflow over Mountains*. WMO Technical Note 34. Geneva: World Meterological Organization, p. 135.

Ralph, F.M., Neiman, P.J., Keller, T.L., Levinson, D. and Fedor, L. (1997) Observations, simulations, and analysis of nonstationary trapped lee waves. *Journal of the Atmospheric Sciences*, 54, 1308–1333. https://doi.org/10.1175/1520-0469(1997)054<1308:OSAAON>2.0.CO;2.

Sauer, J.A., Muñoz-Esparza, D., Canfield, J.M., Costigan, K.R., Linn, R.R. and Kim, Y. (2016) A large-Eddy simulation study of atmospheric boundary layer influence on stratified flows over terrain. *Journal of the Atmospheric Sciences*, 73, 2615–2632. https://doi.org/10.1175/JAS-D-15-0282.1.

Scinocca, J.F. and Peltier, W.R. (1989) Pulsating downslope windstorms. *Journal of the Atmospheric Sciences*, 46(18), 2885–2914. https://doi.org/10.1175/1520-0469(1989)046<2885:PDW>2.0.CO;2.

Scorer, R.S. (1949) Theory of waves in the lee of mountains. *Quarterly Journal of the Royal Meteorological Society*, 75, 41–56. https://doi.org/10.1002/qj.49707532308.

Shutts, G. (1992) Observations and numerical model simulation of a partially trapped lee wave over the Welsh Mountains. *Monthly Weather Review*, 120(9), 2056–2066. https://doi.org/10.1175/1520-0493(1992)120<2056:OANMSO>2.0.CO;2.

Shutts, G. (1997) Operational lee wave forecasting. *Meteorological Applications*, 4(1), 23–35. https://doi.org/10.1017/S1350482797000340.

Smith, C.M. and Skyllingstad, E.D. (2009) Investigation of upstream boundary layer influence on mountain wave breaking and lee wave rotors using a large-eddy simulation. *Journal of the Atmospheric Sciences*, 66, 3147–3164. https://doi.org/10.1175/2009JAS2949.1.

Smith, C.M. and Skyllingstad, E.D. (2011) Effects of inversion height and surface heat flux on downslope windstorms. *Monthly Weather Review*, 139, 3750–3764. https://doi.org/10.1175/2011MWR3619.1.

Smith, R.B. (1985) On severe downslope winds. *Journal of the Atmospheric Sciences*, 42, 2597–2603.

Smith, R.B., Jiang, Q. and Doyle, J.D. (2006) A theory of gravity wave absorption by a boundary layer. *Journal of the Atmospheric Sciences*, 63, 774–781. https://doi.org/10.1175/JAS3631.1.

Smith, R.B. and Kruse, C.G. (2017) Broad-Spectrum Mountain waves. *Journal of the Atmospheric Sciences*, 74(5), 1381–1402. https://doi.org/10.1175/JAS-D-16-0297.1.

Smith, R.B., Nugent, A.D., Kruse, C.G., Fritts, D.C., Doyle, J.D., Eckermann, S.D., Taylor, M.J., Dörnbrack, A., Uddstrom, M., Cooper, W., Romashkin, P., Jensen, J. and Beaton, S. (2016) Stratospheric gravity wave fluxes and scales during DEEPWAVE. *Journal of Atmospheric Sciences*, 73(7), 2851–2869. https://doi.org/10.1175/JAS-D-15-0324.1.

Smith, R.B., Skubis, S., Doyle, J.D., Broad, A.S., Kiemle, C. and Volkert, H. (2002) Mountain waves over Mont Blanc: influence of a stagnant boundary layer. *Journal of the Atmospheric Sciences*, 59, 2073–2092. https://doi.org/10.1175/1520-0469(2002)059<2073:MWOMBI>2.0.CO;2.

Smith, S.A. (2004) Observations and simulations of the November 8, 1999 MAP mountain wave case. *Quarterly Journal of the Royal Meteorological Society*, 130, 1305–1325. https://doi.org/10.1256/qj.03.112.

Soufflet, C., Lott, F. and Damiens, F. (2019) Trapped mountain waves with a critical level just below the surface. *Quarterly Journal of the Royal Meteorological Society*, 145, 1503–1514. https://doi.org/10.1002/qj.3507.

Starr, J.R. and Browning, K.A. (1972) Observations of lee waves by high-power radar. *Quarterly Journal of the Royal Meteorological Society*, 98, 73–85.

Strauss, L., Serafin, S., Haimov, S. and Grubišić, V. (2015) Turbulence in breaking mountain waves and atmospheric rotors estimated from airborne in situ and Doppler radar measurements. *Quarterly Journal of the Royal Meteorological Society*, 141, 3207–3225. https://doi.org/10.1002/qj.2604.

Teixeira, M.A.C. (2017) Diagnosing lee wave rotor onset using a linear model including a boundary layer. *Atmosphere*, 8, 5. https://doi.org/10.3390/atmos8010005.

Teixeira, M.A.C., Argaín, J. and Miranda, P. (2013a) Drag produced by trapped lee waves and propagating mountain waves in a two-layer atmosphere. *Quarterly Journal of the Royal Meteorological Society*, 139, 964–981. https://doi.org/10.1002/qj.2008.

Teixeira, M.A.C., Argaín, J. and Miranda, P. (2013b) Orographic drag associated with lee waves trapped at an inversion. *Journal of the Atmospheric Sciences*, 70(9), 2930–2947.

Teixeira, M.A.C., Miranda, P.M.A. and Valente, M.A. (2004) An analytical model of mountain wave drag for wind profiles with shear and curvature. *Journal of the Atmospheric Sciences*, 61, 1040–1054.

Turnipseed, A.A., Anderson, D.E., Burns, S., Blanken, P.D. and Monson, R.K. (2004) Airflows and turbulent flux measurements in mountainous terrain: part 2: mesoscale effects. *Agricultural and Forest Meteorology.*, 125, 187–205. https://doi.org/10.1016/j.agrformet.2004.04.007.

Udina, M., Soler, M.R. and Sol, O. (2017) A modeling study of a trapped lee-wave event over the Pyrénées. *Monthly Weather Review*, 145, 75–96. https://doi.org/10.1175/MWR-D-16-0031.1.

Viezee W. (1970). An investigation of mountain waves with Lidar observations. Sci. Rept. 1, Contract NAS1-8933, Langley Research Center, Stanford Research Institute, Menlo Park, CA.

Vosper, S.B. (2004) Inversion effects on mountain lee waves. *Quarterly Journal of the Royal Meteorological Society*, 130, 1723–1748. https://doi.org/10.1256/qj.03.63.

Vosper, S.B. (2015) Mountain waves and wakes generated by South Georgia: implications for drag parametrization. *Quarterly Journal of the Royal Meteorological Society*, 141, 2813–2827. https://doi.org/10.1002/qj.2566.

Wagner, J., Dörnbrack, A., Rapp, M., Gisinger, S., Ehard, B., Bramberger, M., Witschas, B., Chouza, F., Rahm, S., Mallaun, C., Baumgarten, G. and Hoor, P. (2017) Observed versus simulated

mountain waves over Scandinavia – improvement of vertical winds, energy and momentum fluxes by enhanced model resolution? *Atmospheric Chemistry and Physics*, 17, 4031–4052. https://doi.org/10.5194/acp-17-4031-2017.

Witschas, B., Rahm, S., Dörnbrack, A., Wagner, J. and Rapp, M. (2017) Airborne wind Lidar measurements of vertical and horizontal winds for the investigation of Orographically induced gravity waves. *Journal of Atmospheric and Oceanic Technology*, 34(6), 1371–1386. https://doi.org/10.1175/JTECH-D-17-0021.1.

Xu, X., Li, R., Teixeira, M.A.C. and Lu, Y. (2021) On the momentum flux of vertically propagating orographic gravity waves excited in nonhydrostatic flow over three-dimensional orography. *Journal of the Atmospheric Sciences*, 78(6), 1807–1822. https://doi.org/10.1175/JAS-D-20-0370.1.

Xue, H. and Giorgetta, M. (2021) A large-eddy simulation study on the diurnally evolving nonlinear trapped lee waves over a two-dimensional steep mountain. *Journal of the Atmospheric Sciences*, 78(2), 399–415. https://doi.org/10.1175/JAS-D-20-0085.1.

Xue, H., Li, J., Qian, T. and Gu, H. (2020) A 100-m-scale modeling study of a gale event on the lee side of a long narrow mountain. *Journal of Applied Meteorology and Climatology*, 59, 23–45. https://doi.org/10.1175/JAMC-D-19-0066.1.

Yang, C., Fu, Z. and Zhao, X. (2013) Analysis of climatic characteristics of gales in complex topographic area. 30th Annual Meeting of the Chinese Meteorological Society, Section P458, p.10.

Zängl, G., Reinert, D., Ripodas, P. and Baldauf, M. (2015) The ICON (ICOsahedral non-hydrostatic) modelling framework of DWD and MPI-M: description of the non-hydrostatic dynamical core. *Quarterly Journal of the Royal Meteorological Society*, 141(687), 563–579. https://doi.org/10.1002/qj.2378.

Zhang, W., Guo, J., Miao, Y., Liu, H., Song, Y., Fang, Z., He, J., Lou, M., Yan, Y., Li, Y. and Zhai, P. (2018) On the summertime planetary boundary layer with different thermodynamic stability in China: a radiosonde perspective. *Journal of Climate*, 31(4), 1451–1465.